



# Enhanced adsorption of lead (II) ions onto cellulose nanoparticles/chitosan composite based on loofah sponge: kinetic and thermodynamic studies

E. A. Matter<sup>1</sup> · Asaad F. Hassan<sup>1</sup> · Nourhan M. Elfaramawy<sup>1</sup> · Ghada Esmail<sup>1</sup>

Received: 18 April 2024 / Revised: 11 May 2024 / Accepted: 30 May 2024  
© The Author(s) 2024

## Abstract

The purpose of this work is to study the efficiency of lead ions removal via adsorption onto created solid nanomaterials. Three solid adsorbents were synthesized as cellulose nanoparticles (CN) extracted from plant loofah sponge using alkali treatment and acid hydrolysis techniques, chitosan beads (CZ), and cellulose nanoparticles/chitosan beads composite (CZC). The generated solid adsorbents were investigated using TGA, N<sub>2</sub> adsorption/desorption, ATR-FTIR spectroscopy, SEM, TEM, XRD, and pH<sub>PZC</sub>. Based on our findings, CZC had a pH<sub>PZC</sub> of 7.2, a larger specific surface area (645.3 m<sup>2</sup>/g), and a total pore volume (0.372 cm<sup>3</sup>/g). The batch adsorption of lead ions was well-fitted by pseudo-second order, Elovich, Langmuir, Temkin, and Dubinin-Radushkevich on all the samples. Cellulose nanoparticles/chitosan composite had the highest Langmuir adsorption capacity (221.104 mg/g) at 47°C, 120 min as shaking time, 2 g/L as adsorbent dose, and pH 6.5. Nitric acid had the highest desorption percentage (92%). The thermodynamic investigation revealed that lead ion adsorption is endothermic, favorable, spontaneous, and physisorption. Our findings showed that CZC has a high adsorption capacity and rapid kinetics, indicating its potential for employment in water treatment.

**Keywords** Cellulose · Loofah sponges · Chitosan · Lead ions · Adsorption

## 1 Introduction

The contamination of metal ions is one of the most significant issues influencing the drinking water quality. Pollution can occur naturally through biogeochemical cycles or from human operations including oil drilling, metal casting, tanning, and chemical industries. Heavy metal ions with their nonbiodegradability, toxicity, nutrient amplification, and bioaccumulation can harm both the environment and humans [1].

Among toxic heavy metals, lead ion is a hazardous heavy metal that can be found in water, soil, and the environment. Lead emissions occur primarily from mining and metal processing, including piston-engine aircraft using electroplating, lead smelters, pigment, and dye manufacture. The increased manufacture of autos and mobile phone batteries

has led to an increase in global Pb (II) output. Lead ions can enter the body through contaminated food and the respiratory system via vapor, dust, and other pollutants. Long-term exposure to Pb (II) ions can negatively impact the kidney, nervous system, and lungs. Further, the permissible amount of Pb (II) in the environment is 0.10–0.30 µg/m<sup>3</sup> [2]. According to the U.S. Environmental Protection Agency (USEPA), the World Health Organization (WHO) and China National Standards (CNS) established maximum acceptable limits for Pb (II) in drinking and surface water are at 15, 10, and 50 µg/L, respectively [3]. As a result, it is crucial to develop innovative materials and effective lead remediation approaches as the pollution problem grows.

Various water treatment strategies were tested for the elimination of lead from polluted water, including chemical precipitation [4], ion exchange [5], electrocoagulation [6], membrane separation [7], photocatalysis [8], bioremediation [9], and adsorption [10–12]. Among them, the adsorption method is an extremely effective approach for eradicating several pollutants. The adsorption process possesses different benefits over water treatment techniques, including simplicity of operation, cost-effectiveness, no hazardous

✉ Asaad F. Hassan  
asmz68@sci.dmu.edu.eg

<sup>1</sup> Chemistry Department, Faculty of Science, Damanhour University, Damanhour, Egypt

byproducts, and high removal efficiency. Furthermore, some adsorbents can also be recycled and reused, lowering overall operational expenses [13]. The process of selecting the appropriate adsorbent was indicated to be complicated. Silica and activated carbon are widely used adsorbents because of their superior capacity to eliminate pollutants from wastewater; nevertheless, they are expensive and have regeneration difficulties. As a result, the emphasis was on generating natural adsorbents from industrial, agricultural, and domestic waste. Lately, numerous natural waste-based adsorbents such as nut shells, hen feathers, leaves, fruit peels, and others produced from agricultural wastes have been explored in the removal of waste contaminants from aqueous medium. Nevertheless, there are progressive efforts to enhance the adsorption effectiveness of natural wastes, making more efficient materials [14, 15].

Cellulose (CN) as the most natural biopolymer with a linear chain having hundreds to thousands of  $\beta$ -1,4 connected D-glucose units and with the formula  $(C_6H_{10}O_5)_n$  is the fundamental building block of plant cell walls, improving their stiffness [16]. Cellulose is extensively utilized, so it is recommended that cellulose can be derived from a sustainable and unconventional source. Loofah sponge (SL) has been discovered to be a feasible source of cellulose and it is a lignocellulose compound consisting of 31% hemicellulose, 58% cellulose, and 11% lignin. SL is a fruit of a fibrovascular system from a subtropical climbing plant in the Cucurbitaceae family. SL has different applications due to its eco-friendliness, morphological and structural features, non-toxicity, high porosity, lightness, biodegradability, and stiffness [17]. Cellulose nanoparticles have been employed as effective adsorbents since they possess an efficient adsorption capacity, wide surface area, low cost, biodegradability, and mechanical strength to eliminate hazardous metal ions. The most efficient technique to synthesize cellulose nanoparticles is acid hydrolysis at particular acid concentrations and temperatures after the alkali treatment for cellulose particles [14]. It can additionally be modified into various functional groups or composites by combining it with other reagents to improve adsorption efficiency.

Chitosan (CZ) is derived from chitin through the deacetylation process, and chitin is the most abundant and cost-effective biopolymer extracted from crab shells. Chitosan has numerous benefits, including biodegradability, antibacterial properties, and biocompatibility. Its amino and hydroxyl functional groups have made it a popular choice for various uses, including medication delivery, agriculture, food preservation, and paper industries. Recently, it has been increasingly employed in wastewater treatment. The presence of amino groups makes it suitable for using as a solid adsorbent, forming complexes with cations or organic molecules. It can be employed in liquid form to coagulate and flocculate complexes of metal ions and anions species [18].

However, chitosan has drawbacks such as a low surface area, poor mechanical capabilities, high solubility in acidic solutions, and deformation after drying. Cross-linking, surface impregnation, and grafting are examples of modifications that can improve adsorption efficiency. Several research investigations have reported modified chitosan adsorbents, which have been thoroughly studied [19]. Nanocomposites have distinctive features such as high adsorption capacity, high thermal stability, high specific surface area, adequate crystallinity, the existence of diverse active sites, and an extremely porous nature to provide the best water treatment. Several biocomposites such as DOTA@sludge@chitosan, DOTA (1,4,7,10-tetraazacyclododecane-N,N',N,N'-tetraacetic acid) [20], a novel composite of glutaraldehyde cross-linked chitosan@acid-activated bentonite (CsG@AAB) [21], cross-linked chitosan-zeolite composite [22], and cellulose/hydroxyapatite/titanium dioxide [23] have been studied and used for lead ion adsorption, where they achieved great adsorption capacity of 329.4, 452.8, 275, and 1012.0 mg/g, respectively. In this study, we prepared cellulose nanoparticles/chitosan composite (CZC) based on a loofah sponge for the first time with excellent characteristics to eliminate Pb (II) ions from wastewater.

The purpose of this research is to (i) extract cellulose nanoparticles (CN) from loofah sponge using alkali treatment and subsequently acid hydrolysis at specific acid concentrations and temperatures, as well as to synthesize chitosan beads (CZ) via precipitation method, and cellulose nanoparticles/chitosan composite (CZC). (ii) ATR-FTIR, XRD, SEM, TEM, TGA, zeta potential, and  $N_2$  adsorption/desorption techniques are used to evaluate surface, physical, and chemical properties. (iii) Analysis of lead adsorption using batch methods was studied under a variety of experimental conditions, including initial concentration of lead, pH, adsorbent dosage, and shaking time. (iv) The adsorption isotherms and kinetics will be carefully examined and modeled. (v) Lead ion desorption from the CZC surface was performed using various eluent solutions, and CZC reusability was examined after five cycles of adsorption/desorption.

## 2 Materials and methods

### 2.1 Materials

Loofah sponge (SL) was harvested from a local farm in Mansoura, Egypt, split into extremely small pieces, rinsed with deionized water to eliminate any contaminants, and then dried in an oven at 85°C. The dried loofah sponge was pulverized into a fine powder with a Retsch ZM200 titanium mill. Lead nitrate was obtained from Sigma-Aldrich, and chitosan was obtained from Piochem Co., Egypt, while hydrochloric acid, sodium hydroxide, acetic acid, chloroform,

sodium hypochlorite, and ethanol were obtained from El-Nasr for Pharmaceutical and Chemical Industry Co., Egypt.

## 2.2 Preparation of solid materials

### 2.2.1 Extraction of cellulose nanoparticles from loofah sponge (CN)

Treatments of alkaline and bleaching were employed to eliminate lignin and hemicellulose from the loofah sponge (SL). 30 g of the milled loofah sponge was treated with 400 mL of NaOH solution (3% w/v, pH 12) at 80°C on a hot plate, stirring continuously for 3 h. The alkali solution was rinsed with distilled water until neutrality and then dried at room temperature for 24 h. The resulting suspension was bleached utilizing 12% sodium hypochlorite at 85°C for 1 h. The sample was washed with distilled water to neutralize the pH and then, dried in an air-circulating oven at 50°C for 12 h. The hydrolysis of SL was performed using 100 mL of 3 mol/L hydrochloric acid at 100°C for 2 h. The hydrolysis reaction was stopped by adding an equivalent volume of cold distilled water to the acidic solution until it became neutral. CN precipitate was suspended in distilled water and dialyzed at room temperature for 3 days. The sample was freeze-dried after being treated with 300 W ultrasonic waves for 20 min in an ice bath to maintain a temperature of 25°C [24].

### 2.2.2 Preparation of chitosan beads (CZ)

Biopolymeric beads were made by dissolving 2 g of chitosan in 200 mL of (2% w/v) acetic acid and stirring continuously at 100 rpm for 2 h. The solution was slowly added to sodium hydroxide solution (2 mol/L) to form chitosan beads (CZ). The formed precipitate was filtered, washed with distilled water several times to remove any contaminants, and dried for 24 h at 75°C [25].

### 2.2.3 Preparation of cellulose nanoparticles/chitosan composite beads (CZC)

The cellulose nanoparticles/chitosan composite with a weight ratio (1:1) was created using the following procedure: briefly, chitosan powder (1 g) was dissolved with 100 mL of (2% w/v) aqueous acetic acid and stirred strongly for 2 h using a magnetic stirrer. Simultaneously, a specific weight of the produced cellulose nanoparticles (1 g) was allowed to undergo partial swelling in a suitable distilled water volume and stirring for 1 h. The cellulose nanoparticle suspension was gradually added to the chitosan solution. The resultant mixture was agitated for 2 h at 60°C until homogeneity, and then slowly injected into 2 mol/L of sodium hydroxide using a syringe. The solid composite was filtered, rinsed with distilled water, and finally dried at 75°C for 24 h.

## 2.3 Characterization of the fabricated solid samples

Thermogravimetric analysis (TGA) was determined by a thermoanalyzer (SDT Q600, V20.9 Build 20). The materials were gradually heated from ambient temperature up to 800°C at 10°C/min. A nitrogen gas flow rate of 50 mL/min was maintained throughout the procedure.

The textural configuration of CN, CZ, and CZC was measured with the NOVA 3200e gas sorption analyzer (Quantachrome Corporation, USA) at  $-196^{\circ}\text{C}$ , which measures the average pore radius  $\bar{r}$  (nm), total pore volume  $V_T$  ( $\text{cm}^3/\text{g}$ ), and specific surface area  $S_{BET}$  ( $\text{m}^2/\text{g}$ ). The crystal arrangement of CN, CZ, and CZC was examined using an X-ray diffractometer (XRD) (D8 advance diffractometer, Germany). The instrument used Cu- $K_{\alpha}$  radiation with a wavelength of 0.154 nm that operated at a current of 44 mA and voltage of 40 kV. X-ray diffraction scans were performed in the 2-theta range ( $10^{\circ}$  to  $80^{\circ}$ ) with a scanning speed of  $1^{\circ}/\text{min}$ .

The functional groups of CN, CZ, and CZC were investigated by using Fourier transform infrared spectroscopy (ATR-FTIR). This analysis was performed by utilizing Nicolet Impact 400 D ATR-FTIR with a ZnSe crystal in transmittance mode between 400 and  $3900\text{ cm}^{-1}$ . To measure  $\text{pH}_{\text{PZC}}$ , zeta potentials of the prepared samples were estimated by Zetasizer Nano S, Malvern Instrument, UK.

The scanning electron microscope (SEM) analysis of the prepared adsorbents was performed using a JEOL JSM-6510LV. The nanosamples were made by collecting them on an aluminum transporter and then coating them with a tiny gold layer at a swerving voltage of 15 kV in an extreme vacuum. Transmission electron microscopy (TEM) was applied to evaluate the morphological structure of CN, CZ, and CZC, employing a JEOL-JEM-2100 model. An anhydrous ethanol solution was chosen to ultrasonically dissolve nano samples for 45 min. The samples were subsequently put on a sheet of copper and allowed to dry for 24 h before being analyzed.

## 2.4 Lead ion batch adsorption

The adsorption of lead ions by all manufactured solid adsorbents (CN, CZ, and CZC) was verified by batch adsorption method through agitating 50 mL of lead solution with a 0.1 g of adsorbent dosage and a specific concentration at pH 6.5 and  $20^{\circ}\text{C}$  with shaking for 120 min. The resulting supernatant was filtered with Whatman filter paper (grade 1). The first 5 mL of the filtrate was discarded and the remaining Pb (II) concentration was detected using an atomic absorption spectrophotometer (GBC Sens. AAS). The equilibrium capacity of adsorption ( $q_e$ , mg/g) and the removal percentage of Pb (II) ( $R\%$ ) were computed using the subsequent calculations (Eqs. 1 and 2), respectively:

$$q_e = (C_o - C_e) \times \frac{V}{W} \quad (1)$$

$$R(\%) = \frac{(C_o - C_e)}{C_o} \times 100 \quad (2)$$

where  $C_e$  and  $C_o$  (mg/L) represent the equilibrium and initial lead ion concentrations, respectively.  $V$  (L) is the volume of lead solution and  $W$  (g) is the adsorbent mass. A variety of adsorption parameters were evaluated to investigate the influence of initial Pb (II) concentration (20–400 mg/L), the adsorbent dosage (0.20–2.38 g/L), shaking time (7–180 min), pH (0.5–8.0), and temperature (20–47°C).

## 2.5 Adsorption kinetics

The kinetic mechanism of lead ion adsorption on CN, CZ, and CZC was studied by applying the nonlinear forms of pseudo-first order (PFO, Eq. 3), pseudo-second order (PSO, Eq. 4), and Elovich (Eq. 5) kinetic models. The adsorption kinetics of Pb (II) ions were investigated by applying adsorption data collected at various time intervals.

$$q_t = q_{exp}(1 - \exp(-k_1 t)) \quad (3)$$

$$q_t = \frac{q_e^2 \cdot k_2 \cdot t}{(1 + k_2 \cdot q_e \cdot t)} \quad (4)$$

$$q_t = \left(\frac{1}{\beta}\right) \ln(1 + \alpha \beta t) \quad (5)$$

Adsorption capacity at a specific point in time ( $q_t$ , mg/g) was expressed using the following equation:

$$q_t = \frac{(C_o - C_t)}{W} \times V \quad (6)$$

Herein, the equilibrium concentration of lead ions at time  $t$ , and the PFO and PSO rate constants are expressed by  $C_t$  (mg/L),  $k_1$  (min<sup>-1</sup>), and  $k_2$  (g/mg·min), respectively. The amounts of lead adsorbed at equilibrium and time  $t$  (min) are portrayed by  $q_e$  and  $q_t$  (mg/g), respectively. Lead ion adsorption's initial rate constant and surface coverage extent are indicated by  $\alpha$  (mg/g·min) as well as  $\beta$  (g/mg), respectively.

## 2.6 Adsorption isotherm

Nonlinear Langmuir (Eq. 7) isotherm states that monolayer adsorbates' adsorption onto an identical surface occurs without collision between the adsorbed molecules. It is assumed that all adsorption sites onto the adsorbent surface possess the same energy and are equivalent. Each site only possesses one molecule [26].

$$q_e = \left(\frac{bC_e}{1 + bC_e}\right) \cdot q_m \quad (7)$$

where the symbols  $q_m$ ,  $b$ , and  $q_e$  stand for maximal adsorption capacity (mg/g), Langmuir constant (L/mg), and adsorption capacity at equilibrium (mg/g), respectively. The separation ( $R_L$ ) factor was employed to ascertain if lead adsorption is favorable ( $0 < R_L < 1$ ), unfavorable ( $R_L > 1$ ), or irreversible ( $R_L = 0$ ). The Langmuir isotherm's separation factor ( $R_L$ ) can be calculated using the following formula:

$$R_L = \frac{1}{1 + b \cdot C_o} \quad (8)$$

Nonlinear Freundlich (Eq. 9) isotherm can be applied to multilayer adsorption with an irregular distribution of thermal energy and interactions throughout the heterogeneous surface [27].

$$q_e = K_F \cdot (C_e)^{\frac{1}{n}} \quad (9)$$

Herein, Freundlich constants ( $K_F$  (L<sup>1/n</sup>·mg<sup>1-1/n</sup>/g) and  $n$ ) are related to the adsorption capacity and intensity, respectively.

Nonlinear Temkin (Eq. 10) isotherm is considered that as surface coverage increases, the heat of adsorption reduces linearly owing to the adsorbate-adsorbent interaction effect [28].

$$q_e = \beta \ln(K_T \cdot C_e) \quad (10)$$

$$\beta = \frac{R}{b_T} T \quad (11)$$

where gas adsorption constant, the absolute temperature, and adsorption heat are represented by the symbols  $R$  (J/mol K),  $T$  (K), and  $\beta$ , respectively. Temkin constants involve  $b_T$  (J/mol) as well as  $K_T$  (L/g).

Nonlinear Dubinin-Radushkevich (Eq. 12) isotherm predicts a multilayer adsorption process including Van der Waal forces. This model differentiates between chemical and physical adsorption of Pb (II) from water [29].

$$q_e = q_{DR} \cdot e^{(-K_{DR} \cdot \epsilon^2)} \quad (12)$$

$$\epsilon = RT \ln\left(1 + \frac{1}{C_e}\right) \quad (13)$$

Here,  $K_{DR}$  (mol<sup>2</sup>/kJ<sup>2</sup>) indicates the activity coefficient,  $\epsilon$  represents Polanyi potential, and  $q_{DR}$  (mg/g) represents the maximal adsorption capacity. The mean free energy ( $E_{DR}$ , kJ/mol) of adsorption is estimated by the following formula:

$$E_{DR} = \frac{1}{\sqrt{2K_{DR}}} \quad (14)$$

## 2.7 Thermodynamic parameters of pb (II) adsorption

The thermodynamic parameters (entropy ( $\Delta S^\circ$ , kJ/mol·K), enthalpy ( $\Delta H^\circ$ , kJ/mol), and the free energy ( $\Delta G^\circ$ , kJ/mol)) changes exhibited an understanding of the adsorption performance. The thermodynamic parameters ( $\Delta H^\circ$  and  $\Delta S^\circ$ ) were determined utilizing the linear Van't Hoff equation (Eq. 15). The Gibbs free energy change was computed using (Eq. 17) [30].

$$\ln K_d = \frac{\Delta S^\circ}{R} - \left( \frac{\Delta H^\circ}{R} \right) \frac{1}{T} \quad (15)$$

$$K_d = \frac{C_s}{C_e} \quad (16)$$

$$\Delta G^\circ = \Delta H^\circ - T\Delta S^\circ \quad (17)$$

Herein, the values of  $\Delta H^\circ$  (kJ/mol) and  $\Delta S^\circ$  (kJ/mol·K) were estimated using the slope and intercept of the Van't Hoff plot, respectively. The concentration of lead ions onto the adsorbent surface and at equilibrium in the solution (mg/L) are denoted by  $C_s$  and  $C_e$ . The adsorption distribution equilibrium constant is denoted by  $K_d$ .

## 2.8 Lead ion desorption and reusability of CZC

The desorption process was examined by combining 0.1 g of CZC with 150 mL of 400 mg/L Pb (II) solution and agitating at 20°C for 2 h. Immediately after adsorption equilibrium, CZC was filtered and carefully rinsed with distilled water to remove any remaining Pb (II). The dried Pb (II) pre-loaded CZC (0.1 g) was combined with 125 mL of several eluents (distilled water, sodium hydroxide, ethanol, chloroform, hydrochloric acid, and nitric acid) for desorption. The resulting mixture was agitated for 24 h and then the concentration of Pb (II) ions in the supernatant was measured. The desorption efficiency percent was determined with the subsequent formula [31]:

$$\text{Desorption efficiency (\%)} = \frac{V \cdot C_d}{m \cdot q} \times 100 \quad (18)$$

where the volume of desorbing agent (L), the lead ion solution concentration after desorption from CZC (mg/L), the adsorbent's adsorption capacity (mg/g), and the weight of solid adsorbent (g) are represented by the symbols  $V$ ,  $C_d$ ,  $q$ , and  $m$ , respectively.

The CZC reusability was applied after five Pb (II) adsorption/desorption runs under the following circumstances: 2 g/L as adsorbent dosage, 300 mg/L of initial lead concentration, pH 7, 60 min as shaking time, and 20°C. After each cycle, CZC was rinsed with distilled water and treated with 45 mL of nitric acid to desorb preabsorbed lead (II) ions for reuse.

## 3 Results and discussion

### 3.1 Characterization of the prepared solid adsorbents

Thermogravimetric analysis was executed to estimate the thermal stability of SL, CN, CZ, and CZC from room temperature to 800°C as displayed in Fig. S1a. Loofah sponge (SL) decomposed through three steps; the first step demonstrated moisture evaporation, resulting in a weight loss of 6.2% from 25 to 150°C. The second stage (190–300°C) included a thermal breakdown of hemicellulose, producing a weight loss of 12.3%. The third stage involved the breaking down of cellulose at temperatures between 320 and 800°C, causing a huge weight loss of 56.3% [32]. The prepared materials (CN, CZ, and CZC) degraded in three thermal degradation phases, the first step displayed about 5.9% (CN), 3.5% (CZ), and 3.9% (CZC) of mass loss at 110°C, relating to the surface adsorbed moisture vaporization. The second phase revealed a weight loss of about 9.8, 16.1, and 22.4% for CN, CZ, and CZC, respectively at temperatures between 200 and 320 °C, belonging to the thermal degradation of cellulose-containing organic carbon in CN and quaternary ammonium groups in CZ besides the hydroxyl groups' oxidation. The last step is up to 800 °C for all the samples with a mass loss of approximately 72.1% for CN which could be attributed to the residual organic matters' decomposition in CN, about 33% for CZ which is attributed to the thermal breakdown of CZ, and about 32.2% for CZC due to polymer chain splitting [33]. The produced nanocomposite is more thermally stable than CN and CZ. The incorporation of CZ with CN increased the thermal stability of CN by the more thermally stable CZ, resulting in a more stable composite.

The nitrogen adsorption-desorption isotherms indicate the structural features (total pore volume ( $V_T$ ), specific surface area ( $S_{BET}$ ), and pore radius ( $\bar{r}$ )) of the manufactured samples, and the data are presented in Table 1. Figure 1a illustrates nitrogen adsorption for CN, CZ, and CZC, where the curves for CN and CZC exhibited type IV with an H3 hysteresis loop behavior, proving the existence of mesoporous structures [21], but chitosan (CZ) demonstrated type II without a hysteresis loop. The data presented in Table 1 show that  $S_{BET}$  and  $V_T$  values of CZC > CZ > CN (645.3, 186.5, and 68.8 m<sup>2</sup>/g) (0.372, 0.210, and 0.165

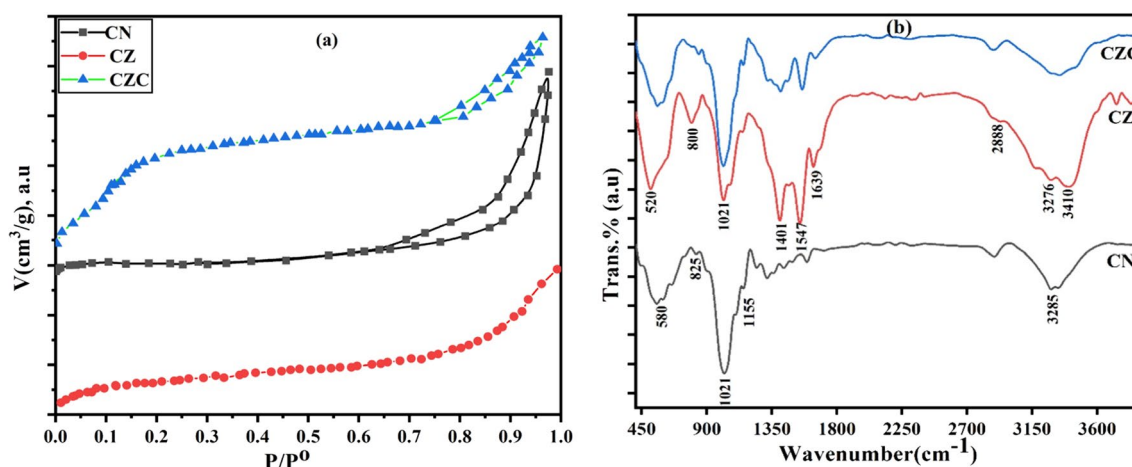


**Fig. 1** Nitrogen adsorption-desorption isotherms (a) and ATR-FTIR curves (b) for CN, CZ, and CZC

$\text{cm}^3/\text{g}$ ), respectively, demonstrating the availability of pores and active sites onto the surface of CZC. The average pore radius ( $\bar{r}$ ) of the solid adsorbents ranged between 20.1 and 46.2 Å, classifying them as mesoporous materials. This mesoporous nature improved the performance of the adsorption process, demonstrating that CN, CZ, and CZC are highly effective adsorbents.

XRD inspection revealed crystal structures and lattice parameters for the prepared solid adsorbents (CN, CZ, and CZC), as shown in Fig. S1b. The XRD pattern of cellulose nanocrystal (CN) exhibits diffraction peaks at  $2\theta$  in the range of 16.0, 22.5, and 34.0°, assigned to the diffraction planes (110), (200), and (004), respectively, which are associated with cellulose-I type [34]. The obtained crystalline peaks at  $2\theta$  value of 22.5° showed the crystalline configuration of cellulose, demonstrating the efficiency of alkaline, bleaching, and hydrolysis treatment in removing the amorphous portions (hemicellulose and lignin), increasing the crystallinity and confirming the purity of CN [35]. The XRD pattern of chitosan (CZ) exhibits a crystalline narrow peak at  $2\theta$  of 21.7°, and an amorphous broad peak at 15.5 and 33.7°, indicating its low crystallinity [36]. The small shift of peaks in CZC composite with high intensity revealed the efficient interaction between two separate polymers (CN and CZ).

The molecular composition of CN, CZ, and CZC was investigated using ATR-FTIR spectroscopy as illustrated in Fig. 1b. The spectra of ATR-FTIR for the prepared solid

adsorbents are at the range 400–3900  $\text{cm}^{-1}$ . ATR-FTIR spectrum of CN shows a broad band at 3285  $\text{cm}^{-1}$  assigned to the stretching vibration of OH groups of CN and the peak at 1155  $\text{cm}^{-1}$  indicated asymmetric COC stretching. The absence of peaks from 1520 to 1740  $\text{cm}^{-1}$  that corresponds to lignin and hemicellulose in CN spectra proves the cellulose purity, and lignin and hemicellulose were efficiently eliminated during the extraction process [35]. The bands noticed at 580 and 825  $\text{cm}^{-1}$  corresponded to a feature of glucose-based linkages of cellulose besides out-of-plane mode of bending for CO-H, and OH stretching in addition to C-H distortion with contributions from ring vibrations, respectively. In the spectra of CN and CZ, the peak at 1021  $\text{cm}^{-1}$  is related to a stretching vibration of the C–O–C pyranose ring [37]. The noticed ATR-FTIR spectrum exhibited distinctive functional groups for chitosan. The peaks in a range from 3276 to 3410  $\text{cm}^{-1}$  are related to the O-H and N-H groups' stretching vibration. The symmetric and asymmetric C-H are indicated by the characteristic peak at 2888  $\text{cm}^{-1}$ . The pyranoses ring stretching vibration is represented by bands at 520 and 800  $\text{cm}^{-1}$  [36]. The bands for N-H bending vibration of amide (II), C=O stretching of amide (I), and C-N stretching of amide (III) appeared at 1547, 1639, and 1401  $\text{cm}^{-1}$ , respectively [38]. The spectrum of CZC revealed distinguishable bands between cellulose nanoparticles and chitosan beads with slight shifts and raised bands' intensity, illustrating the integration of novel

**Table 1** Characterization parameters for the synthesized solid adsorbents

Samples	$\text{pH}_{\text{pzc}}$	$S_{\text{BET}}$ ( $\text{m}^2/\text{g}$ )	$V_T$ ( $\text{cm}^3/\text{g}$ )	$\bar{r}$ (Å)	TEM Average $P_s$ (nm)
CN	4.9	68.8	0.165	46.2	21.3
CZ	7.6	186.5	0.210	21.2	13.5
CZC	7.2	645.3	0.372	20.1	54.8

functional groups on the CZC surface as well as the successful binding between amine and hydroxyl groups of CZ and hydroxyl groups of CN, possibly via hydrogen bonds.

The chemical surface charge of prepared solid adsorbents (CN, CZ, and CZC) was measured by the zeta potential as depicted in Fig. S1c. Table 1 reveals that the values of  $pH_{PZC}$  for CN, CZ, and CZC are 4.9, 7.6, and 7.2, respectively, where at values of  $pH < pH_{PZC}$  and  $> pH_{PZC}$ , the adsorbent surface have positive and negative charges, respectively.

The surface morphology, structure, and shape of the adsorbents (CN, CZ, and CZC) were determined by SEM analysis as shown in Fig. 2a–c, and TEM analysis as depicted in Fig. 2d–f. SEM micrograph in Fig. 2a revealed that the surface of CN is rough with a shape spherical. After alkaline and bleaching treatment, the surface of cellulose becomes rougher. The roughness of cellulose is appropriate for acid hydrolysis to create cellulose nanocrystals. Chemical treatments were efficient in eradicating impurities such as lignin and hemicellulose [37]. This validates the purity of cellulose nanocrystals as indicated in the ATR-FTIR, TGA, and XRD analyses. The surface of CZ as displayed in Fig. 2b seemed as smooth, irregular, nanofiber-structured pores channels on its exterior surfaces, and has an amorphous nature [39]. SEM image of CZC exhibits the improved surface roughness because of the presence of cellulose nanoparticles in the chitosan polymer. A rough surface in composite promoted

better interaction between the adsorbate and the active site of the adsorbent, leading to an increment in adsorption capacity. Figure 2d–f exhibits TEM images of CN, CZ, and CZC that agree with morphology and shape with SEM investigations. CN has the appearance of a spherical and uniform shape with an average particle size of approximately 21.3 nm. TEM micrographs of CZ as shown in Fig. 2e have irregular shapes with average particle size of 13.5 nm. TEM image of CZC composite reveals a distinct incorporation of cellulose nanoparticles and chitosan with a particle size of around 54.8 nm.

## 3.2 The adsorption of pb (II) ions

### 3.2.1 Adsorbent dose impact

Optimizing adsorbent dosage is crucial for efficient Pb (II) treatment. With values ranging from 0.20 to 2.38 g/L, Fig. 3a illustrates the impact of CN, CZ, and CZC masses on the removal percentage ( $R\%$ , Eq. 2) after using 50 mL of Pb (II) concentration (150 mg/L) at 20°C and pH 6.5 for 120 min as a shaking time. It revealed a great increase in  $R\%$  when enhancing the adsorbent amount from 0.2 to 2.0 g/L, where removal percent increased from 3.75, 25.00, and 11.25% to 70.00, 82.50, and 95.00% by 18.7, 3.3, and 8.4 times for CN, CZ, and CZC, respectively, associated

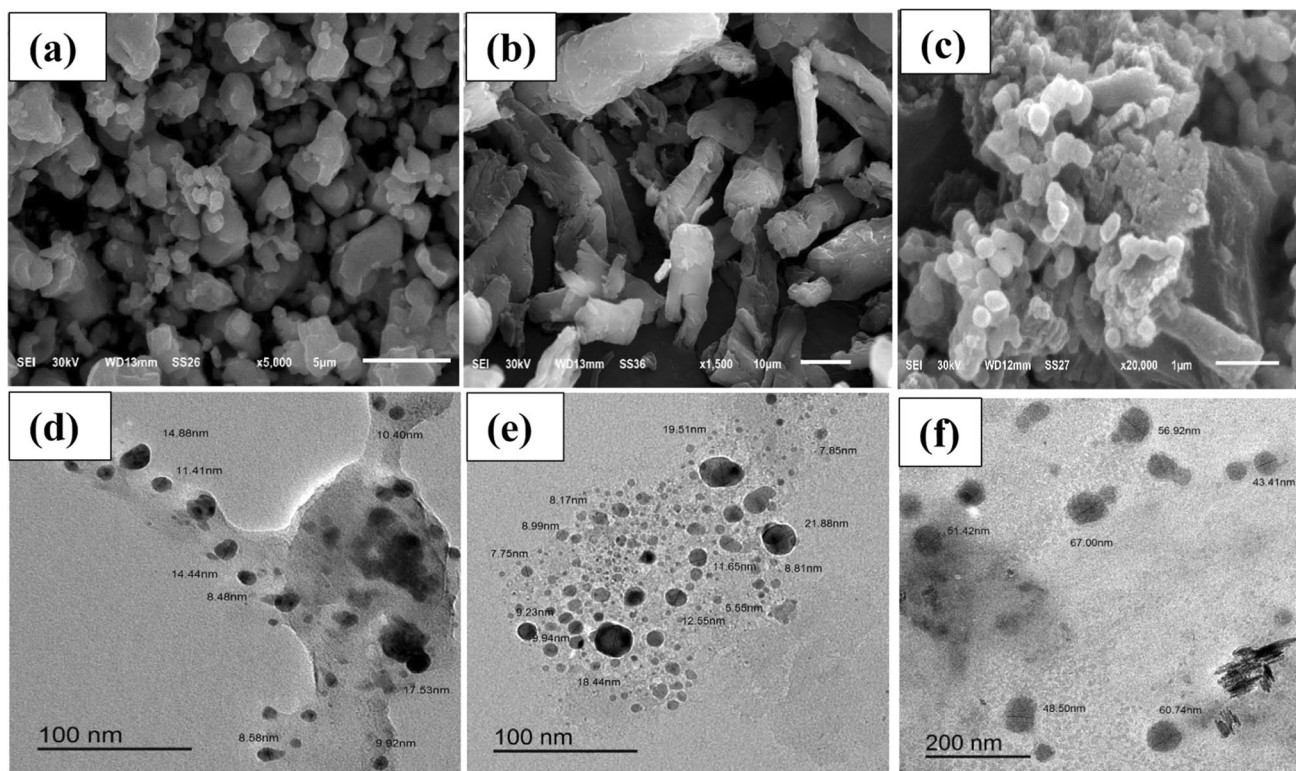


**Fig. 2** SEM images (a, b, c) and TEM images (d, e, f) for CN, CZ, and CZC, respectively

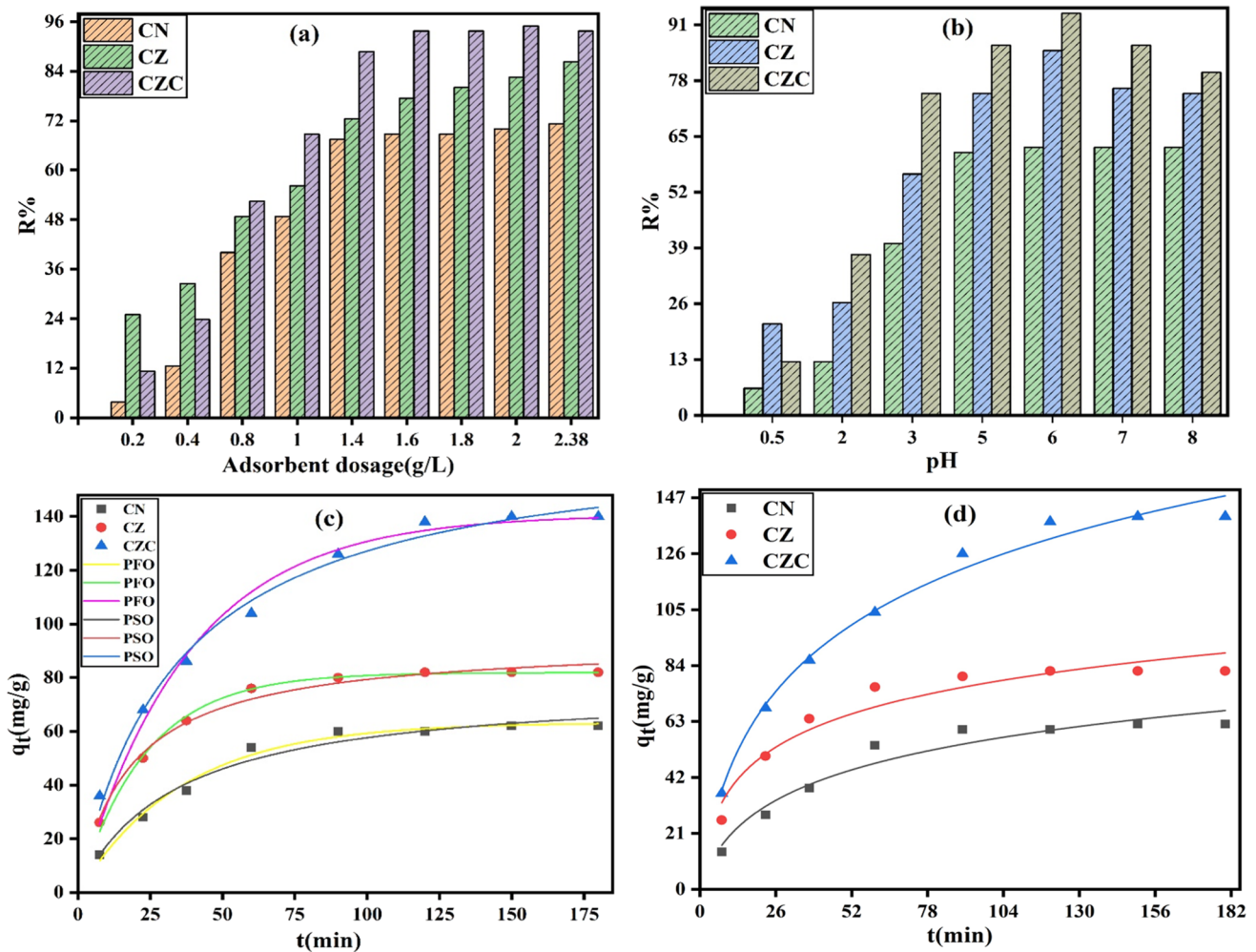


**Fig. 3** Adsorbent dosage (a), pH (b) effects, pseudo-first order and pseudo-second order (c), and Elovich (d) nonlinear plots for Pb (II) adsorption onto CN, CZ, and CZC at 20°C

to the enormous abundance of active adsorption sites onto surfaces [40]. There was no apparent high increase in  $R\%$  at adsorbent doses more than 2 g/L, hence 2 g/L was selected as the optimal dosage for subsequent testing.

### 3.2.2 The impact of initial pH

Electrostatic interaction between adsorbent and adsorbate molecules typically impacts the pH level of the adsorption process. This interaction relies on reducing the functional groups' protonation, which results in changing surface charges at various pH levels [41]. The influence of pH on the removal% of Pb (II) was explored in the range of 0.5–8.0, applying 50 mL of 150 mg/L as initial lead concentration and 2 g/L of adsorbent dosage at 20°C for 120 min of agitating time as depicted in Fig. 3b. Declined removal percent for all the solid adsorbents was obvious at acidic values of pH, attributing to the elevated proton levels, which competed

with Pb (II) for attraction to the limited active sites of the adsorbent materials [42]. A rise in pH from 0.5 to 6.0 significantly improved the removal efficiency for CN, CZ, and CZC by 10.0, 4.0, and 7.5 times, respectively. Increasing the pH to 6 considerably decreased the concentration of  $H^+$  and anticipated competition between  $H^+$  and Pb (II). Furthermore, the negative charges onto the surface of adsorbents increased considerably, improving electrostatic interactions between the adsorbents and Pb (II) cations [2]. CZC composite had the highest removal percent, exhibiting an abundance of functional surface groups due to the successful binding between the cellulose nanoparticles and chitosan. The small decrease in Pb (II) elimination at  $pH > 6$  is attributed to Pb (II) hydrolysis in the forms of a precipitate as  $Pb(OH)_2$  or a complex as  $[Pb(OH)_3]^-$  and  $[Pb(OH)]^+$ , decreasing the concentration of free Pb (II) ions in the solution and reducing the adsorbent binding strength to lead ions, lowering the removal efficiency [43, 44].



### 3.2.3 Kinetics of lead adsorption

Adsorption kinetic shows the time necessary for the adsorption equilibrium and adsorption mechanism. The most appropriate adsorption duration was selected by plotting contact time (min) against the adsorption capacity ( $q_t$ , mg/g, Eq. 6) of the synthesized samples for the removal of lead ions in the range of 7–180 min, consuming 50 mL of 150 mg/L as initial lead concentration and 0.1 g of adsorbent dose at pH 6.5 and 20°C as shown in the dots of Fig. 3c, d. The adsorption capacity of CN, CZ, and CZC increased rapidly by 3.85, 2.92, and 2.89 times, respectively in the first 60 min, owing to the existence of abundant adsorption sites onto the adsorbent surface at the start of adsorption [45]. Subsequently, Pb (II) adsorption slowly declined and finally reached equilibrium because of the saturation of active sites and the reducing strength of driving force toward the adsorbent surface [46]. Figure 3c conveys the PFO (Eq. 3) and PSO (Eq. 4) nonlinear graphs, while Elovich (Eq. 5) nonlinear graph is depicted in Fig. 3d. Additionally the kinetic parameters for Pb (II) adsorption onto solid materials are listed in Table 2. Based on the data in Table 2, PSO was determined to be the ideal candidate for fitting lead ion adsorption onto the tested adsorbents (CN, CZ, and CZC) based on its higher correlation coefficients ( $R^2$ ) > 0.9898 and a relatively small difference (2.8, 0.3, and 3.6% for CN, CZ, and CZC, respectively) between the computed adsorption capacity ( $q_{exp}$ ) of PSO and that calculated via Langmuir ( $q_m$ ) model. PFO cannot be applied

because of significant disparities between estimated  $q_{exp}$  and Langmuir values (28.5, 10.4, and 27.6% for CN, CZ, and CZC, respectively), and also, the  $R^2$  values (0.9550–0.9738) are less than those of PSO. The correlation coefficients of Elovich kinetic model ranged from 0.9229 to 0.9846, showing that it is widely applicable. The  $\alpha$  and  $\beta$  values for lead adsorption on CN, CZ, and CZC are in the range of 3.5110–11.6034 mg/g·min and 0.0243–0.0532 g/mg, respectively, illustrating the rapid surface covering process [47].

### 3.2.4 Adsorption isotherm modeling

The initial concentration of lead ions is the primary factor in determining the behavior of adsorption process. The influence of the initial concentration of lead ions in the range from 20 to 400 mg/L on lead removal on CN, CZ, and CZC was investigated using 2 g/L as an adsorbent dosage at 20°C and pH 6.5 for 120 min of agitating time as shown in the dots of graphs of Fig. 4a–c. The increase in adsorption capacity ( $q_e$ , mg/g, Eq. 1) occurred at the beginning of the increase in initial Pb (II) concentrations. The reason for that increase is that at a lower initial lead concentration, the active sites of adsorbents are sufficient to hold the metal ions. The adsorption capacity then began to stabilize at a high initial concentration because the available active sites were saturated, indicating that the adsorption capacities for lead ions' removal reached their maximum [48].

Various models of adsorption isotherm were employed to determine Langmuir (Eq. 7) and Freundlich (Eq. 9) isotherms as depicted in the nonlinear forms in Fig. 4a–c, while Temkin (Eq. 10) and Dubinin-Radushkevich (Eq. 12) models are shown in the nonlinear forms in Figs. 4d–f and 5a–c, respectively. Table 3 shows the calculated parameters. According to the data in Table 3, (i) the adsorption of lead ions on all the generated adsorbents was well fitted by Freundlich and Langmuir adsorption models, exhibiting uniform and heterogeneous monolayer-multilayer adsorption of lead ions onto the surface of adsorbents based on the elevated correlation coefficients ( $R^2$  > 0.9274) at various temperatures. The Langmuir model has greater correlation coefficient values (0.9824–0.9964) than the Freundlich model (0.9274–0.9726), indicating that the Langmuir model is more applied than the Freundlich model. (ii) The adsorption capacity of CZC > CZ > CN by 41.1 and 51.3%, respectively, compared with CZC at 47°C, revealing the greater surface area of CZC (645.3 m<sup>2</sup>/g) and the existence of novel surface functional groups. The rise in adsorption capacity as temperature increased from 20 to 47°C validated the endothermic behavior of the adsorbed lead ion on CN, CZ, and CZC. (iii) The values of dimensionless separation factor ( $R_L$ , Eq. 8) between 0 and 1 are favorable for the adsorption of lead ions on the produced solid samples [49]. (iv) Langmuir constant ( $b$ , L/mg) values were

**Table 2** Pseudo-first, pseudo-second order, Elovich kinetic models at 20°C, and thermodynamic parameters for lead adsorption onto CN, CZ, and CZC samples

Models	Parameters	CN	CZ	CZC	
PFO	$q_m$ (mg/g)	86.628	91.390	188.812	
	$q_{exp}$ (mg/g)	61.865	81.911	136.599	
	$k_1$ (min <sup>-1</sup> )	0.0277	0.0431	0.0265	
	$R^2$	0.9663	0.9738	0.9550	
PSO	$q_{exp}$ (mg/g)	84.209	91.130	182.004	
	$k_2 \times 10^{-4}$ (g/mg·min)	3.814	5.938	1.711	
	$R^2$	0.9898	0.9942	0.9982	
Elovich	$\alpha$ (mg/g·min)	3.511	11.603	8.044	
	$\beta$ (g/mg)	0.0527	0.0532	0.0243	
	$R^2$	0.9398	0.9229	0.9846	
Thermo-dynamic parameters	$R^2$	0.9679	0.9862	0.9837	
	$\Delta H^\circ$ (kJ/mol)	22.872	14.961	17.467	
	$\Delta S^\circ$ (kJ/mol·K)	0.0871	0.0672	0.0792	
	$-\Delta G^\circ$ (kJ/mol)	20°C	2.648	4.729	5.739
		30°C	3.519	5.401	6.531
	40°C	4.390	6.073	7.323	
	47°C	5.000	6.543	7.877	

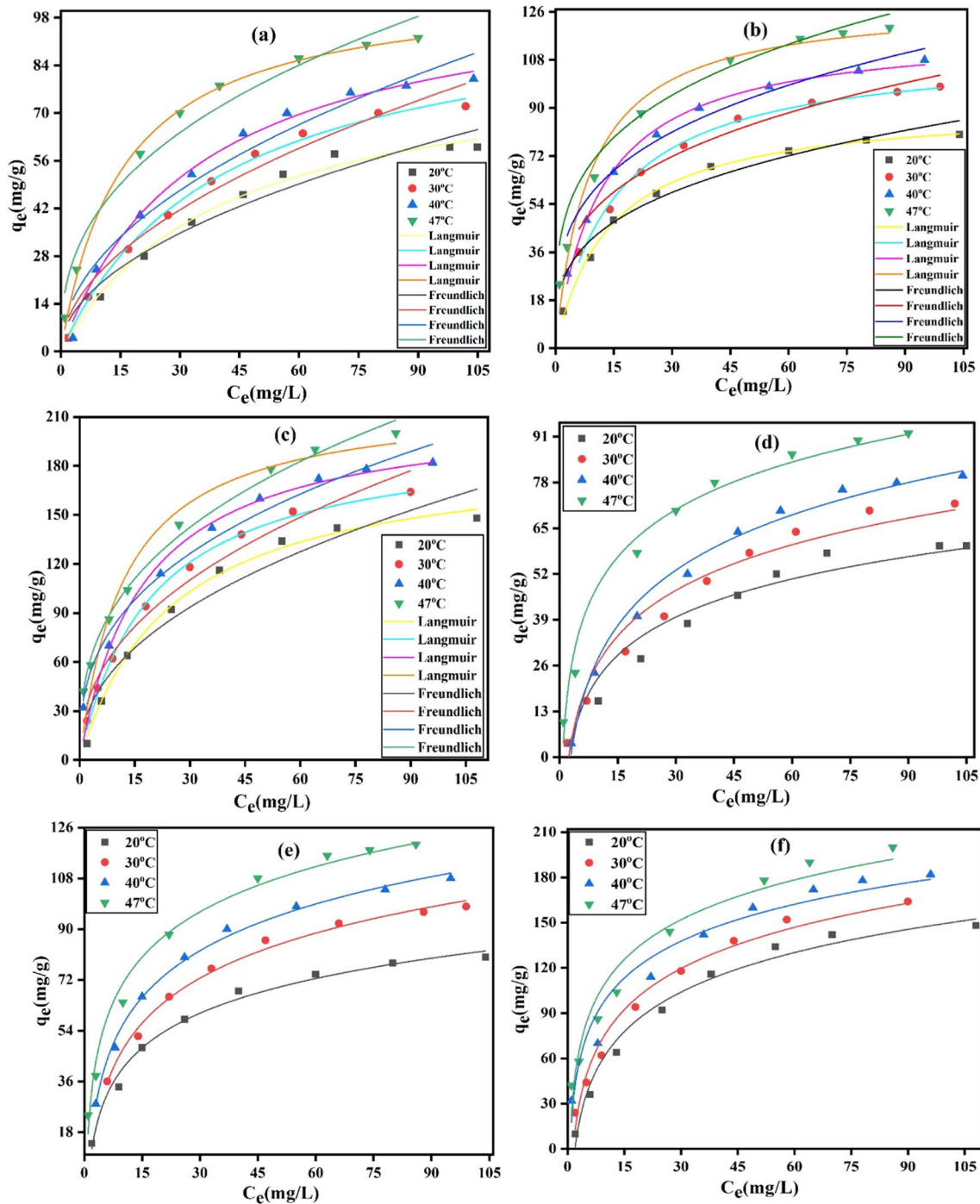


**Fig. 4** Langmuir and Freundlich (a, b, c), and Temkin isotherm model (d, e, f) nonlinear plots for the adsorption of Pb (II) onto CN, CZ, and CZC, respectively, at 20, 30, 40, and 47°C

observed in the sequence  $CZ > CZC > CN$  at all the studied temperatures as shown in Table 3, showing an elevated attraction of lead ions to the adsorption sites of CZ, especially at 47°C. The values of  $1/n$  ranged between 0.2645 and 0.5212 ( $0 < 1/n < 1$ ), illustrating favorability of lead adsorption [50]. The values of  $n$  ( $> 1$ ) confirm the physical characteristics of the adsorption process [51].

The nonlinear graphs of Temkin model for lead ion adsorption onto CN, CZ, and CZC at different temperatures (20, 30, 40, and 47°C) are depicted in Fig. 4d–f; Table 3 illustrates the parameters of Temkin isotherm. According to the findings in Table 3,  $R^2$  values vary from 0.9607 to 0.9953 for all solid materials at different temperatures, proving the well-fitted Temkin isotherm model. The

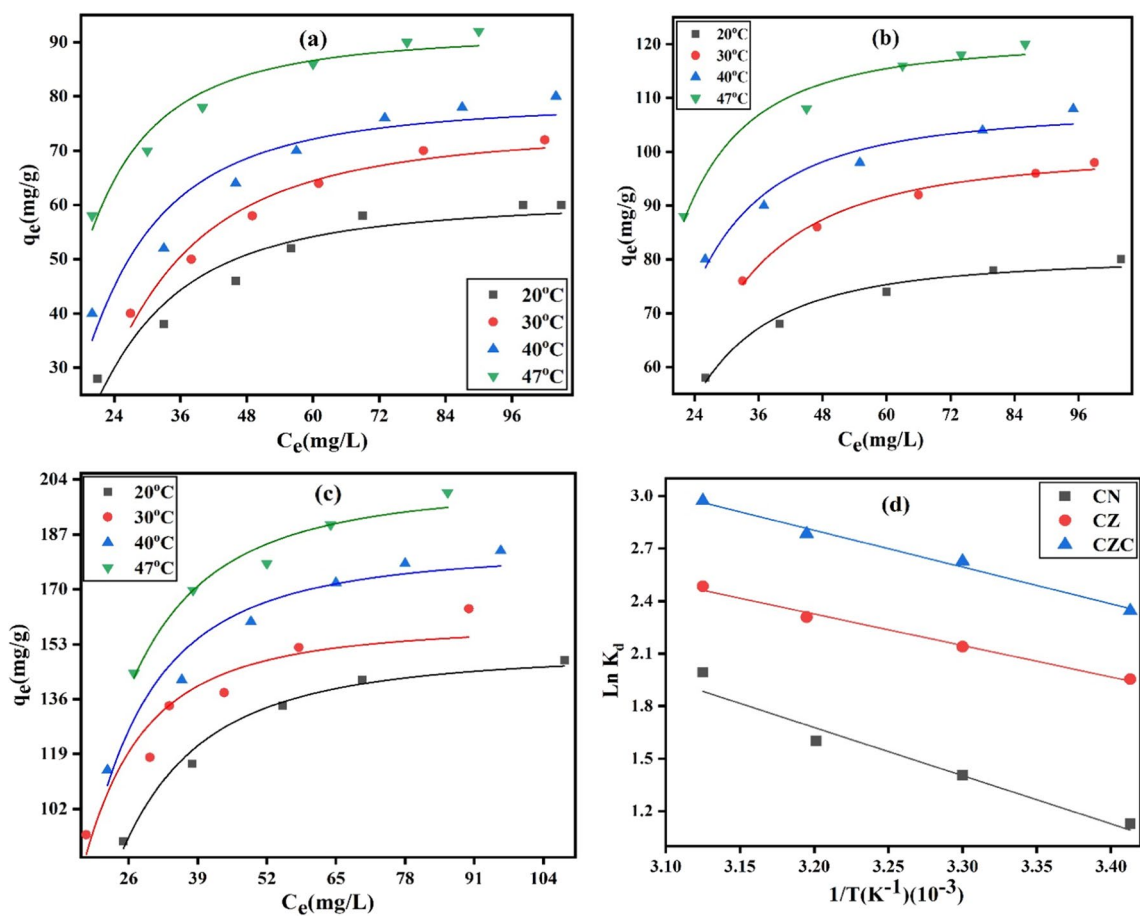


Fig. 5 The nonlinear Dubinin-Radushkevich model (a, b, c) plots for CN, CZ, and CZC, respectively, at 20, 30, 40, and 47°C and Van't Hoff plot (d) for all the solid adsorbent.

Table 3 Langmuir, Freundlich, Temkin, and Dubinin-Radushkevich parameters for lead adsorption onto CN, CZ, and CZC at 20, 30, 40, and 47°C

Parameters	CN				CZ				CZC			
	20°C	30°C	40°C	47°C	20°C	30°C	40°C	47°C	20°C	30°C	40°C	47°C
Langmuir												
$q_m$ (mg/g)	86.628	103.648	109.438	107.698	91.130	112.267	119.457	130.255	188.812	199.152	214.712	221.104
$b$ (L/mg)	0.0244	0.0247	0.0291	0.0641	0.0713	0.0669	0.0845	0.1133	0.0400	0.0516	0.0581	0.0827
$R_L$	0.2907	0.2882	0.2557	0.1349	0.1230	0.1300	0.1058	0.0811	0.2000	0.1623	0.1468	0.1079
$R^2$	0.9907	0.9964	0.9920	0.9958	0.9962	0.9922	0.9952	0.9869	0.9949	0.9963	0.9839	0.9824
Freundlich												
$1/n$	0.5025	0.5212	0.4943	0.3877	0.3049	0.2963	0.2835	0.2645	0.4467	0.4318	0.3655	0.3598
$K_F$	6.284	7.058	8.797	17.184	20.698	26.218	30.876	38.556	20.468	25.361	36.435	41.879
$R^2$	0.9335	0.9463	0.9380	0.9431	0.9327	0.9353	0.9312	0.9274	0.9332	0.9479	0.9603	0.9726
Temkin												
$K_T$ (L/g)	0.4252	0.4207	0.3467	1.2379	0.9894	0.7817	1.0494	2.1257	0.5183	0.6911	1.6444	1.7975
$b_T$ (J/mol)	155.901	134.836	114.792	136.777	137.256	109.469	109.022	115.051	64.302	63.866	73.658	69.816
$R^2$	0.9607	0.9753	0.9889	0.9899	0.9873	0.9905	0.9953	0.9854	0.9892	0.9892	0.9682	0.9707
Dubinin-Radushkevich												
$q_{DR}$ (mg/g)	62.679	75.702	81.543	93.437	81.355	100.680	109.564	122.139	152.606	164.338	185.789	205.582
$E_{DR}$ (kJ/mol)	0.0853	0.0800	0.1020	0.1324	0.1134	0.1018	0.1256	0.1500	0.0958	0.1284	0.1169	0.1178
$R^2$	0.9426	0.9633	0.9466	0.9600	0.9700	0.9836	0.9665	0.9751	0.9812	0.9411	0.9564	0.9766

lower values of Temkin parameter ( $b_T < 8000$  J/mol) ranged from 63.866 to 155.901 J/mol, confirming the physical Pb (II) adsorption onto the employed materials. Additionally, the trend of  $b_T$  values (CN > CZ > CZC) means that CZC required less heat throughout the adsorption process [52].

Figure 5a–c depicts the nonlinear graphs of Dubinin-Radushkevich (DR) isotherm for lead ion adsorption on CN, CZ, and CZC at different temperatures (20, 30, 40, and 47°C). Depending on the data in Table 3, the estimated values of  $R^2$  of DR model are more than 0.9411, confirming lead ion adsorption was well applied by Dubinin-Radushkevich isotherm. The mean free energy ( $E_{DR}$ , kJ/mol) is employed to identify the kind of adsorption if  $E_{DR} < 8$  kJ/mol, the process is physical adsorption, and if  $8 < E_{DR} < 16$  kJ/mol, ion exchange or chemical adsorption is the fundamental process [53]. As mentioned in the current study, the values of  $E_{DR}$  are in the range of 0.0800 to 0.1500 kJ/mol, suggesting the physisorption of lead ions. As a result of the above findings, the Langmuir, Freundlich, Temkin, and Dubinin-Radushkevich models fitted well with lead ion adsorption.

### 3.2.5 Thermodynamic parameters

The lead ions' adsorption by the produced solid samples (CN, CZ, and CZC) was investigated at various temperatures (20, 30, 40, and 47°C). Table 2 demonstrates that (i) the Van't Hoff model (Eq. 15) as shown in Fig. 5d was effectively applied with elevated correlation coefficients (0.9679 for CN, 0.9862 for CZ, and 0.9837 for CZC). (ii) The endothermic nature of Pb (II) adsorption onto the prepared adsorbents was proved by the positive enthalpy ( $\Delta H^\circ$ ) values (22.872, 14.961, and 17.467 kJ/mol for CN, CZ, and CZC, respectively). (iii) Positive entropy changes ( $\Delta S^\circ$ ) values (0.0871, 0.0672, and 0.0792 kJ/mol·K for CN, CZ, and CZC, respectively) indicated the increased disorder of Pb (II) ions during adsorption at the solid-liquid interface [54]. (iv) The negative Gibbs

free energy change ( $\Delta G^\circ$ ) values reveal that the adsorption process is spontaneous. The calculated values of  $\Delta G^\circ$  are significantly negative from 20 to 47°C, implying that increasing temperature is favorable for lead ion adsorption as a result of a stronger driving force of adsorption [55]. Changes in  $\Delta G^\circ$  values from  $-80$  to  $-400$  and  $0$  to  $-20$  kJ/mol indicate chemical and physical adsorption processes, respectively. Thus, the  $\Delta G^\circ$  values ( $-2.648$  to  $-7.877$  kJ/mol) assert the physical adsorption of Pb (II) ions [56].

The mechanism of Pb (II) adsorption onto the prepared composite (CZC) can be directly ascribed to the chemical functional groups of the CZC composite (Fig. S2). The formed composite was distinguished by different functional groups on its surface including hydroxyl, amino, and ketone groups which improved electrostatic interactions or surface complexation of their lone pair of electrons with cationic Pb (II) ions as a physical adsorption [57–59].

### 3.3 Desorption studies and the reusability of solid adsorbent

The desorption efficiency ( $D.E\%$ ) was estimated utilizing Eq. 18. Figure 6a shows the desorption efficiency of several eluents (92% for nitric acid, 45% for hydrochloric acid, 15% for ethanol, 12% for water, 8% for sodium hydroxide, and 4% for chloroform). The values of  $D.E\%$  depend on the polarity and viscosity of the eluents, the quantity of produced cations (particularly protons) from eluents, and the lead ions' solubility in the desorbing agent. The interactions between lead ions and CZC surface were mostly physical binding forces. Chloroform and NaOH had the lowest desorption percentages due to their low concentrations of positively charged protons, while  $\text{HNO}_3$  and HCl had the maximum desorption efficiency due to the increased quantity of protons in acidic media based on the acidity constant, increasing the electrostatic repulsion between lead ions and protonated sites on CZC surface [51].

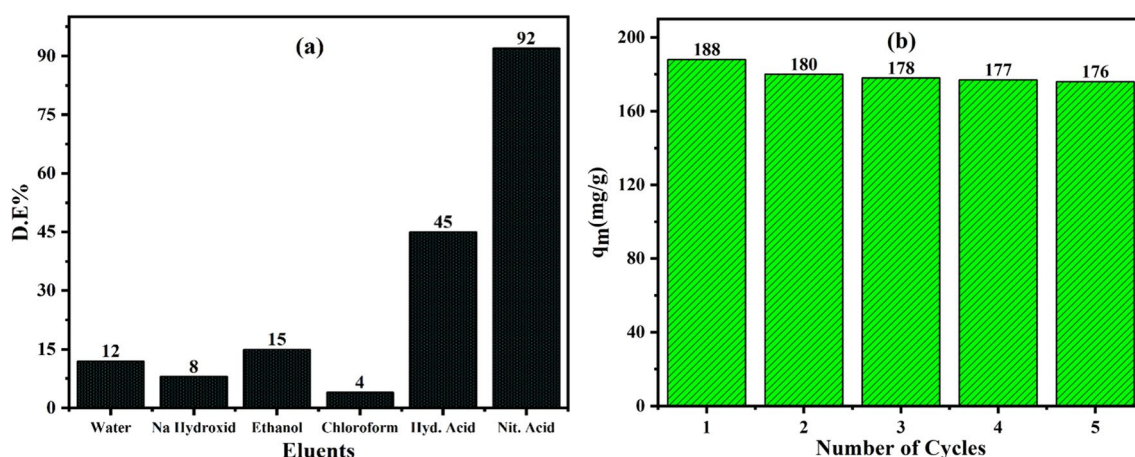


Fig. 6 Desorption of lead ions from CZC using different eluents (a) and CZC reusability after five cycles of adsorption/desorption (b)

**Table 4** Comparison of CZC maximum adsorption capacity with other materials

Adsorbents	$q_m$ (mg/g)	References
Granular activated carbon-doped Mg-Al LDH composites (MgAl@AC)	94.57	[13]
Chitosan/CaCO <sub>3</sub> -NPs nanocomposite (Cs/CaCO <sub>3</sub> -NC)	98.03	[18]
Bentonite/amino-functionalized cellulose composite (BAC)	69.00	[29]
Modified bark eucalyptus	175.02	[49]
Terephthalate-ZnAl-LDH	124.00	[55]
Araucaria gum/calcium alginate composite beads (CR11)	149.95	[56]
CZC	221.10	[Present study]

The reusability of CZC throughout five cycles of lead ion adsorption/desorption is shown in Fig. 6b. After five consecutive cycles of regeneration, CZC showed a small decline in adsorption efficiency by only 6.4%. The reduction in adsorption efficiency could be related to the decline in specific surface area and the predicted loss of some chemical functional groups onto the surface [60].

### 3.4 Comparison between CZC efficiency with other adsorbents

Table 4 shows that CZC has the maximum adsorption capacity compared to other adsorbents [13, 18, 29, 49, 55, 56]. CZC composite is an efficient adsorbent to eliminate Pb (II) ions from wastewater through batch adsorption.

## 4 Conclusion

Applying natural adsorbents in polluted water remediation systems is an efficient technology for the removal of metal ions from wastewater. The present work explored the elimination of lead ions from water in static adsorption techniques, employing adsorbents like cellulose nanoparticles extracted from the plant loofah sponge (CN) using alkali treatment and acid hydrolysis, chitosan beads (CZ), and cellulose nanoparticles/chitosan beads composite (CZC). CZC exhibited a highly thermal stability, a maximum specific surface area of 645.3 m<sup>2</sup>/g, a total pore volume of 0.372 cm<sup>3</sup>/g, a mesoporous radius of 20.1 Å, and an average particle size of 54.8 nm. The precise integration of chitosan pellets into cellulose nanoparticles by composite synthesis created special chemical functional groups on the CZC composite by combining the hydroxyl and amino groups of CZ and the hydroxyl groups of CN, causing greater activity at surface sites and forming more exterior pores. Experimental adsorption showed that CZC had the greatest adsorption capacity of Langmuir model, using 2 g/L of adsorbent dosage for 120 min of shaking time at pH 6.5 and 47°C. Where adsorption capacity of CZC (221.104 mg/g) > CZ (130.255 mg/g) > CN (107.698 mg/g) by 41.1 and 51.3%, respectively, compared to CZC at 47°C, revealing the existence of novel surface functional groups and greater surface

area of CZC. The Elovich, pseudo-second order, Langmuir, Freundlich, Temkin, and Dubinin-Radushkevich models effectively applied lead ion adsorption on the studied adsorbents. This study indicated that lead ion adsorption was endothermic, spontaneous, favorable, and physisorption. Nitric acid has the highest desorption efficiency percent (92%). The enhanced reusability of CZC composite was investigated using five runs of lead ions adsorption/desorption with just a 6.4% loss of its adsorption efficiency. Previous studies have shown that CZC has excellent and distinctive adsorption characteristics in wastewater remediation.

**Supplementary Information** The online version contains supplementary material available at <https://doi.org/10.1007/s13399-024-05800-1>.

**Author contribution** All authors contributed to the study conception and design. Material preparation, data collection, and analysis were performed by E. A. Matter, Asaad F. Hassan, Nourhan M. Elfaramawy, and Ghada Esmail.

**Funding** Open access funding provided by The Science, Technology & Innovation Funding Authority (STDF) in cooperation with The Egyptian Knowledge Bank (EKB).

## Declarations

**Conflict of interest** The authors declare no competing interests.

**Open Access** This article is licensed under a Creative Commons Attribution 4.0 International License, which permits use, sharing, adaptation, distribution and reproduction in any medium or format, as long as you give appropriate credit to the original author(s) and the source, provide a link to the Creative Commons licence, and indicate if changes were made. The images or other third party material in this article are included in the article's Creative Commons licence, unless indicated otherwise in a credit line to the material. If material is not included in the article's Creative Commons licence and your intended use is not permitted by statutory regulation or exceeds the permitted use, you will need to obtain permission directly from the copyright holder. To view a copy of this licence, visit <http://creativecommons.org/licenses/by/4.0/>.

## References

- Gomes EJCM, Macedo VS, dos Santos Pereira AK et al (2024) Theoretical study of the adsorption capacity of potentially toxic Cd<sup>2+</sup>, Pb<sup>2+</sup>, and Hg<sup>2+</sup> ions in hemicellulose matrices. *Int J Biol Macromol* 258:128894. <https://doi.org/10.1016/j.ijbiomac.2023.128894>

2. Omer AM, El-Sayed M, Abd El-Monaem EM et al (2023) Graphene oxide@Fe<sub>3</sub>O<sub>4</sub>-decorated iota-carrageenan composite for ultra-fast and highly efficient adsorption of lead (II) from water. *Int J Biol Macromol* 253:127437. <https://doi.org/10.1016/j.ijbiomac.2023.127437>
3. Peng S-Y, Lin Y-W, Lin Y-Y, Lin K-L (2024) Hydrothermal synthesis of hydroxyapatite nanocrystals from calcium-rich limestone sludge waste: Preparation, characterization, and application for Pb<sup>2+</sup> adsorption in aqueous solution. *Inorg Chem Commun* 160:111943. <https://doi.org/10.1016/j.inoche.2023.111943>
4. Zheng E, Feng G, Jiang F et al (2024) Effect of process parameters on the synthesis and lead ions removal performance of novel porous hydroxyapatite sheets prepared via non-aqueous precipitation method. *Ceram Int*. <https://doi.org/10.1016/j.ceramint.2023.12.406>
5. Rong Y, Yan W, Wang Z et al (2023) Rapid and selective removal of pb ions by electroactive titanium dioxide/polyaniline ion exchange film. *Sep Purif Technol* 312:123386. <https://doi.org/10.1016/j.seppur.2023.123386>
6. Choudhary V, Goyal H, Varma AK et al (2023) Life cycle assessment (LCA) of the lead, chromium, and cadmium removal from water through electrocoagulation. *Mater Today Proc*. <https://doi.org/10.1016/j.matpr.2023.08.297>
7. Alotaibi KM, Shukla AK, Bajuayfir E et al (2023) Ultrasound-assisted synthesis of MSNs/PS nanocomposite membranes for effective removal of Cd<sup>2+</sup> and Pb<sup>2+</sup> ions from aqueous solutions. *Ultrason Sonochem* 98:106497. <https://doi.org/10.1016/j.ultsonch.2023.106497>
8. Song L, Ouyang R, Xu X et al (2024) Photocatalytic degradation of rhodamine B and removal of Pb<sup>2+</sup> over an all-day-active carbon nitride. *Next Mater* 2:100057. <https://doi.org/10.1016/j.nxmate.2023.100057>
9. Chen Z, Liu H, Wang H et al (2024) Flue gas PbO removal from sludge incineration through biological lead oxidation coupled denitrification. *Fuel* 355:129500. <https://doi.org/10.1016/j.fuel.2023.129500>
10. Zhang Y, Li A, Tian T et al (2024) Preparation of amino functionalized magnetic oyster shell powder adsorbent for selective removal of anionic dyes and pb (II) from wastewater. *Int J Biol Macromol* 260. <https://doi.org/10.1016/j.ijbiomac.2024.129414>
11. Chen Q, Zhang Y, Xia H et al (2023) Fabrication of two novel amino-functionalized and starch-coated CuFe<sub>2</sub>O<sub>4</sub>-modified magnetic biochar composites and their application in removing Pb<sup>2+</sup> and Cd<sup>2+</sup> from wastewater. *Int J Biol Macromol* 258:128973. <https://doi.org/10.1016/j.ijbiomac.2023.128973>
12. El Mouden A, El Messaoudi N, El Guerraf A et al (2023) Removal of cadmium and lead ions from aqueous solutions by novel dolomite-quartz@Fe<sub>3</sub>O<sub>4</sub> nanocomposite fabricated as nanoadsorbent. *Environ Res* 225:115606. <https://doi.org/10.1016/j.envres.2023.115606>
13. Khalil AKA, Almanassra IW, Chatla A et al (2023) Insights into the adsorption of lead ions by Mg-Al LDH doped activated carbon composites: implications for fixed bed column and batch applications. *Chem Eng Sci* 281:119192. <https://doi.org/10.1016/j.ces.2023.119192>
14. Musa A, Ibrahim Zakari M, Lawal Mashi A, Saleh TA (2023) Preparation of nanocomposite of zinc oxide with nanocrystalline cellulose from Luffa sponge for removal of metronidazole from aqueous solutions. *Environ Nanotechnol Monit Manag* 20:100840. <https://doi.org/10.1016/j.enmm.2023.100840>
15. El Messaoudi N, Çiğeroğlu Z, Şenol ZM et al (2024) Green synthesis of CuFe<sub>2</sub>O<sub>4</sub> nanoparticles from bioresource extracts and their applications in different areas: a review. *Biomass Convers Biorefinery*. <https://doi.org/10.1007/s13399-023-05264-9>
16. Khorasani AC, Satvati PR (2024) Reusable cellulose-based biosorbents for efficient iodine adsorption by economic microcrystalline cellulose production from walnut shell. *Int J Biol Macromol* 256:128432. <https://doi.org/10.1016/j.ijbiomac.2023.128432>
17. da Costa JS, Fajardo AR (2023) Polypyrrole/stearic acid-coated Luffa cylindrica for enhanced removal of sodium diclofenac from water: batch and continuous adsorption studies. *J Clean Prod* 389. <https://doi.org/10.1016/j.jclepro.2023.136084>
18. Hassan SSM, El-Aziz MEA, Fayed AES et al (2024) Synthesis and characterization of bio-nanocomposite based on chitosan and CaCO<sub>3</sub> nanoparticles for heavy metals removal. *Int J Biol Macromol* 255:128007. <https://doi.org/10.1016/j.ijbiomac.2023.128007>
19. Anvari S, Hosseini M, Jahanshahi M, Banisheykholeslami F (2024) Design of chitosan/boehmite biocomposite for the removal of anionic and nonionic dyes from aqueous solutions: adsorption isotherms, kinetics, and thermodynamics studies. *Int J Biol Macromol* 259:129219. <https://doi.org/10.1016/j.ijbiomac.2024.129219>
20. Xu K, He T, Li L et al (2024) DOTA functionalized adsorbent DOTA@Sludge@Chitosan derived from recycled shrimp shells and sludge and its application for lead and chromium removal from water. *Int J Biol Macromol* 255:128263. <https://doi.org/10.1016/j.ijbiomac.2023.128263>
21. El Kaim Billah R, Islam MA, Nazal MK et al (2024) A novel glutaraldehyde cross-linked chitosan@acid-activated bentonite composite for effective Pb (II) and Cr (VI) adsorption: experimental and theoretical studies. *Sep Purif Technol* 334:126094. <https://doi.org/10.1016/j.seppur.2023.126094>
22. Şenol ZM, Elma E, El Messaoudi N, Mehmeti V (2023) Performance of cross-linked chitosan-zeolite composite adsorbent for removal of Pb<sup>2+</sup> ions from aqueous solutions: experimental and Monte Carlo simulations studies. *J Mol Liq* 391:123310. <https://doi.org/10.1016/j.molliq.2023.123310>
23. Xuchao P, Yong H, Semirumi DT et al (2023) Development of cellulose/hydroxyapatite/TiO<sub>2</sub> scaffolds for efficient removal of lead (II) ions pollution: characterization, kinetic analysis, and artificial neural network modeling. *Int J Biol Macromol* 246:125630. <https://doi.org/10.1016/j.ijbiomac.2023.125630>
24. Ebrahimi R, Fathi M, Ghoddusi HB (2024) Pickering emulsions stabilized by cellulose nanocrystals extracted from hazelnut shells: production and stability under different harsh conditions. *Int J Biol Macromol* 258:128982. <https://doi.org/10.1016/j.ijbiomac.2023.128982>
25. Oliveira RVM, Maia HB, Costa JAS, Romão LPC (2024) Chitosan-based magnetic bioadsorbent beads from eucalyptus sawdust waste for the direct Violet-51 dye remediation: eco-friendly strategy and statistical optimization. *Int J Biol Macromol* 254. <https://doi.org/10.1016/j.ijbiomac.2023.127764>
26. de Oliveira JT, Estumano DC, Féris LA (2024) Resolution methods for adsorption models, batch and continuous mode, and its impact on process implementation: an experimental and statistical comparison. *J Water Process Eng* 58:104888. <https://doi.org/10.1016/j.jwpe.2024.104888>
27. Verma Y, Sharma G, Kumar A et al (2024) Synthesizing pectin-crosslinked gum ghatti hydrogel for efficient adsorptive removal of malachite green. *Int J Biol Macromol* 258:128640. <https://doi.org/10.1016/j.ijbiomac.2023.128640>
28. Feitosa AG, Tatiane da Costa Santos Y, Menezes JMC et al (2023) Evaluation of Pb<sup>2+</sup> ion adsorption by roasted and grounded barley (*Hordeum vulgare* L.) waste. *Results Chem* 6:101205. <https://doi.org/10.1016/j.rechem.2023.101205>
29. Obsa AL, Shibeshi NT, Mulugeta E, Workeneh GA (2024) Bentonite/amino-functionalized cellulose composite as effective adsorbent for removal of lead: kinetic and isotherm studies. *Results Eng* 21:101756. <https://doi.org/10.1016/j.rineng.2024.101756>
30. Steffens BC, Segala BN, Tanabe EH et al (2024) Adsorption and desorption strategy for recovering β-carotene from crude

- palm oil: kinetics, equilibrium and thermodynamics studies. *Food Bioprod Process* 143:158–169. <https://doi.org/10.1016/j.fbp.2023.11.002>
31. Zanin Lima J, Monici Raimondi Nauerth I, Ferreira da Silva E et al (2023) Competitive sorption and desorption of cadmium, lead, and zinc onto peat, compost, and biochar. *J Environ Manage* 344:118515. <https://doi.org/10.1016/j.jenvman.2023.118515>
  32. da Costa JS, Fajardo AR (2023) Polypyrrole/stearic acid-coated *Luffa cylindrica* for enhanced removal of sodium diclofenac from water: batch and continuous adsorption studies. *J Clean Prod* 389:136084. <https://doi.org/10.1016/j.jclepro.2023.136084>
  33. Ibrahim AS, Gad AN, Dardeer HM, Gaber A-AM (2023) Chitosan-cellulose nanocomposite: preparation, characterization, and evaluation as cationic color precipitant in sugar clarification process. *Food Chem* 415:135603. <https://doi.org/10.1016/j.foodchem.2023.135603>
  34. El-Fattah WA, Guesmi A, Ben Hamadi N et al (2024) A green synthesis of cellulose nanocrystals biosorbent for remediation of wastewater containing industrial dye. *Colloids Surf Physicochem Eng Asp* 681:132729. <https://doi.org/10.1016/j.colsurfa.2023.132729>
  35. Amirah Badi NS, Zul Hilmey Makmud M, Se Mun C et al (2024) Synthesis and characterization of cellulose nanocrystal derived from paper as nanofiller for polymer insulation materials. *Mater Today Proc*. <https://doi.org/10.1016/j.matpr.2023.12.059>
  36. Jiang X, Yu Y, Ma S et al (2024) Chitosan nanoparticles loaded with *Eucommia ulmoides* seed essential oil: preparation, characterization, antioxidant and antibacterial properties. *Int J Biol Macromol* 257:128820. <https://doi.org/10.1016/j.ijbiomac.2023.128820>
  37. Ebrahimi R, Fathi M, Ghodusi HB (2024) Pickering emulsions stabilized by cellulose nanocrystals extracted from hazelnut shells: production and stability under different harsh conditions. *Int J Biol Macromol* 258:128982. <https://doi.org/10.1016/j.ijbiomac.2023.128982>
  38. Bhatia S, Shah YA, Al-Harrasi A et al (2024) Novel applications of black pepper essential oil as an antioxidant agent in sodium caseinate and chitosan based active edible films. *Int J Biol Macromol* 254:128045. <https://doi.org/10.1016/j.ijbiomac.2023.128045>
  39. Charii H, Boussetta A, Ait Benhamou A et al (2024) Exploring the potential of chitin and chitosan extracted from shrimp shell waste in enhancing urea-formaldehyde wood adhesives. *Int J Adhes Adhes* 129:103599. <https://doi.org/10.1016/j.ijadhadh.2023.103599>
  40. El Mouden A, El Guerraf A, El Messaoudi N et al (2022) Date stone functionalized with 3-aminopropyltriethoxysilane as a potential biosorbent for heavy metal ions removal from aqueous solution. *Chem Afr* 5:745–759. <https://doi.org/10.1007/s42250-022-00350-3>
  41. Georgin J, Franco DSP, Manzar MS et al (2024) A critical and comprehensive review of the current status of 17 $\beta$ -estradiol hormone remediation through adsorption technology. Springer, Berlin Heidelberg
  42. Aljohani MS, Alnoman RB, Alharbi HY et al (2024) Designing of a cellulose-based ion-imprinted biosorbent for selective removal of lead (II) from aqueous solutions. *Int J Biol Macromol* 259:129145. <https://doi.org/10.1016/j.ijbiomac.2023.129145>
  43. Das J, Rawat A, Chaudhary M et al (2024) Development of novel heteroatoms enriched nanoporous material for rapid removal of pb(II) ions from water bodies by batch adsorption and cross-flow membrane filtration method. *J Water Process Eng* 58:104823. <https://doi.org/10.1016/j.jwpe.2024.104823>
  44. Yuan M, Liu D, Liu W et al (2024) Graphene oxide/polydopamine modified montmorillonite/carboxymethyl chitosan composite aerogel for efficient removal of Pb<sup>2+</sup>, Cu<sup>2+</sup>, and Cd<sup>2+</sup>: adsorption behavior, mechanism and DFT study. *Sep Purif Technol* 339:126585. <https://doi.org/10.1016/j.seppur.2024.126585>
  45. Cigeroğlu Z, El Messaoudi N, Şenol ZM et al (2024) Clay-based nanomaterials and their adsorptive removal efficiency for dyes and antibiotics: a review. *Mater Today Sustain* 26. <https://doi.org/10.1016/j.mtsust.2024.100735>
  46. Li J, Lin G, Zhong Z et al (2024) A novel magnetic Ti-MOF/chitosan composite for efficient adsorption of pb(II) from aqueous solutions: synthesis and investigation. *Int J Biol Macromol* 258:129170. <https://doi.org/10.1016/j.ijbiomac.2023.129170>
  47. Hassan AF, El-Naggar GA, Braish AG et al (2023) Fabrication of titania/calcium alginate nanocomposite matrix for efficient adsorption and photocatalytic degradation of malachite green. *Int J Biol Macromol* 249:126075. <https://doi.org/10.1016/j.ijbiomac.2023.126075>
  48. Ijaz I, Bukhari A, Nazir A et al (2024) Enhanced selective adsorption capacity of lead (II) from complex wastewater by aminopropyltriethoxysilane-functionalized biochar grafted on the MXene based on anion-synergism. *Mater Chem Phys* 314:128929. <https://doi.org/10.1016/j.matchemphys.2024.128929>
  49. Mustapha LS, Obayomi OV, Yahya MD et al (2024) Exploring the synergistic effects of calcium chloride modification on stem bark eucalyptus biochar for cr(VI) and pb(II) ions removal: kinetics, isotherm, thermodynamic and optimization studies. *Bioresour Technol Rep* 25:101699. <https://doi.org/10.1016/j.biteb.2023.101699>
  50. Yang L, Bao L, Zhong Y et al (2024) Fabrication of in situ metal-organic framework grown on sodium lignosulphonate hydrogel for removal of Pb<sup>2+</sup>, methylene blue and crystal violet from aqueous solution. *J Clean Prod* 434:139831. <https://doi.org/10.1016/j.jclepro.2023.139831>
  51. Hassan AF, El-Naggar GA, Esmail G, Shaltout WA (2023) Efficient adsorption of methylene blue on novel triple-nanocomposites of potassium Kappa-carrageenan, calcium alginate and nano-hydroxyapatite obtained from sea scallop shells. *Appl Surf Sci Adv* 13:100388. <https://doi.org/10.1016/j.apsadv.2023.100388>
  52. Khamwicht A, Dechapanya W, Dechapanya W (2022) Adsorption kinetics and isotherms of binary metal ion aqueous solution using untreated venus shell. *Heliyon* 8:e09610. <https://doi.org/10.1016/j.heliyon.2022.e09610>
  53. Yadav S, Das J, Chaurasia SP et al (2024) Amine-functionalized single-layered 2D nanosheets of  $\alpha$ -zirconium phosphate for highly efficient removal of Pb<sup>2+</sup> ions and Congo red dye. *Chem Eng Sci* 285:119628. <https://doi.org/10.1016/j.ces.2023.119628>
  54. Li Y, Xie L, Qu G et al (2024) Efficient treatment of palladium from wastewater by acrolein cross-linked chitosan hydrogels: adsorption, kinetics, and mechanisms. *Int J Biol Macromol* 254:127850. <https://doi.org/10.1016/j.ijbiomac.2023.127850>
  55. de Aquino RVS, de Lucena PGC, Arias S et al (2024) Influence of terephthalate anion in ZnAl layered double hydroxide on lead ion removal: adsorption, kinetics, thermodynamics and mechanism. *Colloids Surf Physicochem Eng Asp* 686:133404. <https://doi.org/10.1016/j.colsurfa.2024.133404>
  56. Khoj MA, Hassan AF, Awwad NS et al (2024) Fabrication and characterization of Araucaria gum/calcium alginate composite beads for batch and column adsorption of lead ions. *Int J Biol Macromol* 255:128234. <https://doi.org/10.1016/j.ijbiomac.2023.128234>
  57. Wang Y, Huang Z, Sheng L et al (2022) Adsorption of lead ions from aqueous solution using NH<sub>4</sub>H<sub>2</sub>PO<sub>4</sub> modified humic acid residue. *Environ Technol Innov* 28:102920. <https://doi.org/10.1016/j.eti.2022.102920>
  58. Sirijaree T, Praipipat P (2023) Adsorption of lead (II) ions onto goethite chitosan beads: isotherms, kinetics, and mechanism studies. *ChemEngineering* 7:. <https://doi.org/10.3390/chemengineering7030052>

59. Chen Y, Shi J, Rong H et al (2020) Adsorption mechanism of lead ions on porous ceramsite prepared by co-combustion ash of sewage sludge and biomass. *Sci Total Environ* 702:135017. <https://doi.org/10.1016/j.scitotenv.2019.135017>
60. Kotnala S, Bhushan B, Nayak A (2024) Hydroxyapatite@cellulose@nZVI composite: fabrication and adsorptive removal of doxycycline, cr(VI) and as(III) from wastewater. *Chem Eng Sci* 288:119796. <https://doi.org/10.1016/j.ces.2024.119796>

**Publisher's Note** Springer Nature remains neutral with regard to jurisdictional claims in published maps and institutional affiliations.